AGU ADVANCING EARTH AND SPACE SCIENCE

Key Points:
- Mars' mobile CO_2 inventory on obliquity timescales is ~100 millibar, with adsorptive regolith exchange down to >~200 m to <~1 km depth
- Mars' peak surface pressure is ~40% lower with best-fit regolith adsorption parameters than when adsorption is ignored
- The product of depth and specific surface area is most important regolith property influencing the polar CO_2 ice stratigraphy

Obliquity-Driven CO₂ Exchange Between Mars' Atmosphere, Regolith, and Polar Cap

P. B. Buhler[1,2] and S. Piqueux[1]

[1]Jet Propulsion Laboratory, California Institute of Technology, Pasadena, CA, USA, [2]Now at Planetary Science Institute, Tucson, AZ, USA

Abstract Discerning the total mass of Mars' obliquity-timescale (~10^5-year) exchangeable CO_2 inventory has been elusive for decades due to the unknown adsorptive capacity of its regolith. Now, however, the stratigraphy of Mars' recently discovered South Polar Massive CO_2 Ice Deposit (MCID) provides a record of orbit-driven CO_2 exchange between its polar cap, atmosphere, and regolith with sufficient constraint to calculate the adsorptive capacity of its regolith and therefore the total mass of its exchangeable CO_2 inventory. We use a numerical climate model and Markov Chain Monte Carlo analysis to show that the observed MCID stratigraphic record is most consistent with a mobile CO_2 inventory of $3.8^{+3.0}_{-1.2} \times 10^{17}$ kg (100^{+80}_{-34} mbar, 68% confidence interval) that exchanges on obliquity timescales. We find that adsorptive CO_2 exchange with the regolith on obliquity timescales likely occurs in the depth range of >~200 m to <~1 km, with the deeper bound set by thermal processes and adsorptive surface availability. Our best-fit model yields a peak mean annual surface pressure 40% lower than CO_2 exchange models that neglect an adsorbing regolith. We provide machine-readable text files of our results to aid future study of Mars' climate.

Plain Language Summary Mars' atmosphere is primarily CO_2. In addition to atmospheric CO_2, Mars also has a polar CO_2 ice cap and a reservoir of CO_2 adsorbed in its regolith (i.e., CO_2 molecules forming a thin film on martian soil grains). Determining how much total CO_2 exchanges between the atmosphere, cap, and regolith over orbit-driven climate cycles is important for understanding Mars' climatic evolution. We constructed a climate model to calculate how CO_2 exchanges between the atmosphere, cap, and regolith over these ~10^5-year cycles. The model outputs a predicted thickness of alternating layers of CO_2 and H_2O ice in the CO_2 ice cap. Comparing our model results to the observed layering of the polar cap indicates that ~100 millibars of CO_2 (~$17\times$ the current atmospheric mass) can exchange between the atmosphere, polar cap, and regolith during these cycles. Moreover, regolith adsorption likely decreases Mars' peak atmospheric pressure by ~40%, which implies that near-surface habitable environments with liquid water are more difficult to create and sustain on Mars than previously thought.

1. Introduction

Mars has three CO_2 reservoirs that exchange on obliquity (~10^5 year) timescales: the atmosphere, the South Polar Massive CO_2 Ice Deposit (MCID), and CO_2 adsorbed in the regolith. Mars' current atmosphere is 96% CO_2 by mass, with a ~6.4 mbar average surface pressure that varies by ±~15% due to seasonal deposition and sublimation of CO_2 ice at the poles (Hess et al., 1980; Owen et al., 1977). The MCID is a CO_2 ice deposit overlying Mars' principally H_2O ice South Polar Layered deposits that has a mass approximately equal to that of the atmosphere (Bierson et al., 2016; Phillips et al., 2011; Putzig et al., 2018). The MCID reaches up to 1 km thickness and contains three identified layers of H_2O ice (Bierson et al., 2016, Figure 1). The existence of CO_2 adsorbed in the Martian regolith was proposed by Fanale and Cannon (1971) and later demonstrated by the Viking Lander 1 Gas Exchange Experiment (Ballou et al., 1978; Oyama & Berdahl, 1977). Modeling studies undertaken prior to the discovery of the MCID have suggested that the adsorbed CO_2 inventory may constitute ~26 mbar (Zent & Quinn, 1995)–~500 mbar (Fanale et al., 1982).

As Mars' orbit evolves, CO_2 exchanges between these reservoirs due to changes in the mean annual latitudinal distribution of sunlight (e.g., Fanale et al., 1982). Mars' orbital evolution also more generally drives climate change (e.g., Toon et al., 1980). However, climate studies typically neglect CO_2 adsorption because
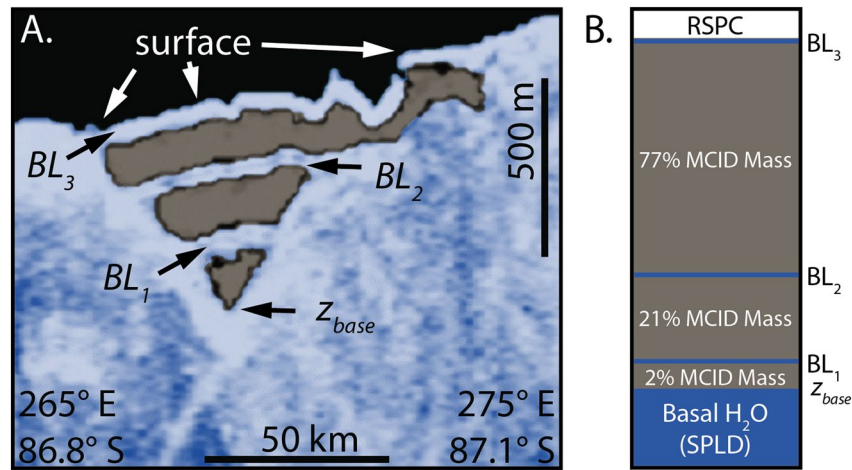
Figure 1. (a) Colorized radargram (interpretation: CO_2 gray, H_2O blue) modified from Buhler et al. (2020) with H_2O ice "Bounding Layers" (BL) and latitude-longitude end points. (b) Stratigraphic layer masses (CO_2 gray, H_2O blue) derived from Bierson et al. (2016), including the Residual South Polar Cap (RSPC, white). Note that the surface RSPC layer is too thin to be seen in the radargram.

the extent and mass of the adsorbed CO_2 reservoir is unconstrained by observation, even though adsorbed CO_2 may significantly affect Mars' pressure history (e.g., Fanale et al., 1982). The present study investigates CO_2 exchange on obliquity timescales.

Previous attempts to model the obliquity-timescale mobile inventory of CO_2 did not have the benefit of comparison to the record of CO_2 exchange stored in the MCID stratigraphy (e.g., Fanale et al., 1982; Zent & Quinn, 1995). Instead, they relied on the best observations of the time, which indicated that Mars had an insignificant polar CO_2 ice deposit. As a result, the task of identifying the obliquity-timescale mobile inventory of CO_2 was both fit to an incorrect present-day distribution of Martian CO_2 reservoirs and also under-constrained, requiring previous investigators to select their preferred value of regolith adsorptive capacity (a term used throughout this report to mean the product of regolith thickness and specific surface area).

Fortunately, the MCID provides a geologic record of CO_2 exchange between the atmosphere, MCID, and regolith (Bierson et al., 2016; Buhler et al., 2020; Manning et al., 2019). The modern observations of the MCID available to us provide a more accurate understanding of Mars' present-day distribution of CO_2 reservoirs. Additionally, the ability to make use of the observed ratio of multiple MCID layers (rather than the binary presence/absence of a polar CO_2 ice deposit) sufficiently constrains statistical determination of the best-fit parameters, eliminating the need to select regolith adsorptive capacity as a model input.

As of yet, there has been no systematic investigation of how CO_2 adsorption affects the MCID geologic record. Here, we perform a numerical modeling investigation to assess how the presence of adsorbed CO_2 reservoirs of various sizes affect the MCID stratigraphic record and compare these predictions to the observed stratigraphy of the MCID. These modeling investigations both elucidate the physical processes by which adsorbed CO_2 affects the MCID stratigraphy and allow us to estimate the magnitude of the regolith adsorptive capacity and adsorbed CO_2 mass relevant to CO_2 exchange on obliquity timescales (Section 3). We discuss our findings in Section 4.

2. Methods

We adopt a general framework in which changes to Mars' mean annual latitudinal insolation, due to Mars' orbital evolution, thermodynamically drive the exchange of CO_2 between the atmosphere, MCID, and regolith. That is, the MCID and atmosphere are always in vapor contact (Buhler et al., 2020) and there is not kinetic hindrance of CO_2 exchange between the atmosphere and regolith on timescales relevant to Mars' orbital variations (Toon et al., 1980). Additionally, we assume that the layer of H_2O ice capping the MCID is permeable to CO_2 exchange between the atmosphere and the MCID (Buhler et al., 2020; Phillips et al., 2011),
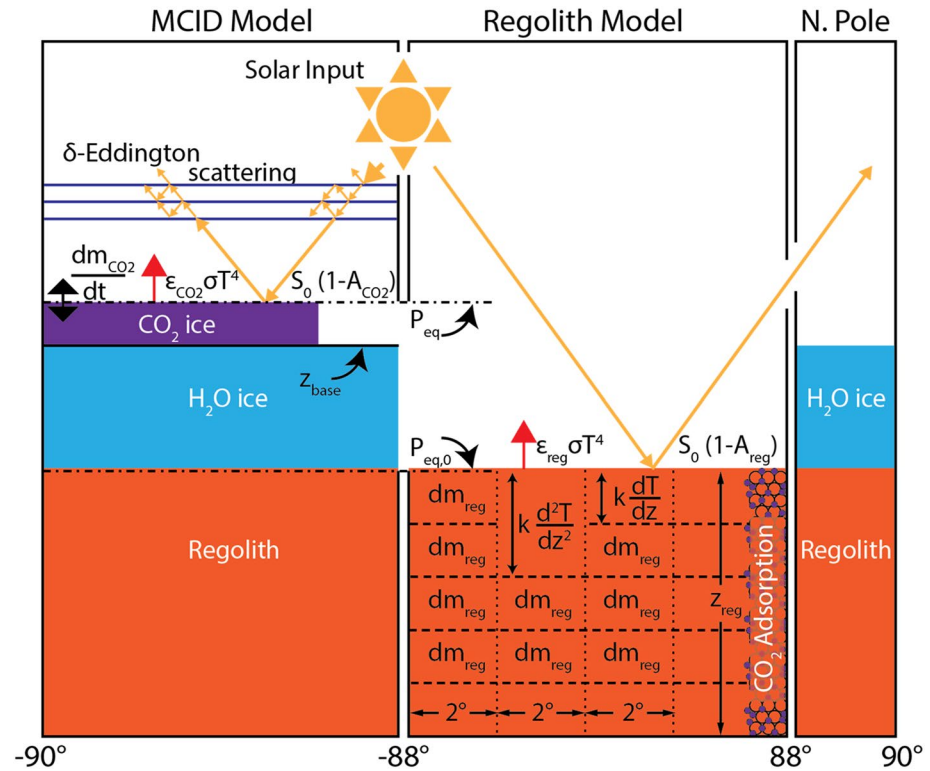
Figure 2. Schematic model. Latitude markings indicate the spatial regime of each part of the model. Left panel depicts treatment of massive CO_2 ice deposit (MCID) energy balance and vapor pressure equilibrium. Note z_{base} is the interface between the MCID and the underlying H_2O ice deposit and is fixed to the elevation of the observed interface in the model. P_{eq} is calculated at the elevation of the top of the MCID, which varies with the amount of CO_2 in the MCID. The center panel depicts the adsorbed CO_2 treatment of surface energy balance, subsurface thermal conduction, and calculation of adsorbed CO_2. Surface pressure $P_{eq,0}$ is calculated at Mars' zero-elevation datum, scaled from P_{eq}. The north polar region (right panel) is modeled using the same physics as the south polar region, but our model finds that no perennial CO_2 cap forms in the north so, in practice, this region is inert in the model. k_{reg} is abbreviated as k in the illustration for visual clarity.

although we note that some studies suggest the MCID might be sequestered (Bierson et al., 2016; Manning et al., 2019).

We perform numerical simulations of CO_2 exchange between the atmosphere, MCID, and regolith to investigate the history of CO_2 cycling between these reservoirs as Mars' orbital elements evolve (Laskar et al., 2004). In our model, the atmospheric CO_2 is in contact with both the regolith and the MCID, while the MCID and regolith exchange CO_2 indirectly, through the atmosphere (Figure 2).

2.1. CO_2 Exchange Between the Atmosphere and the MCID

In our model, CO_2 partitioning between the atmosphere and MCID is set according to (Buhler et al., 2020):

$$P_{eq,cap} = P_{eq,0} \exp\left[-\frac{z_{base} + \dfrac{m_{cap}}{a_{cap}\rho_{CO_2}}}{H}\right] \qquad (1)$$

Here, $P_{eq,cap}$ is the equilibrium pressure at the elevation of the upper surface of the MCID. $P_{eq,0}$ is the pressure at the zero-elevation datum, which is also the mean elevation of the top of the regolith. Throughout this study, we report $P_{eq,0}$ as a multiple of the current zero-elevation pressure. We take the current

atmospheric mass to be $m_{atm} = 2.75 \times 10^{16}$ kg, the mean of the masses calculated by Haberle et al. (2008) and Guo et al. (2010).

The exponential term in Equation 1 is an isothermal atmospheric approximation of pressure decrease as a function of altitude. z_{base} is the elevation of the basal interface of the MCID with the underlying South Polar Layered Deposit (SPLD, an ~3 km-thick unit composed of dirty H_2O ice; e.g., Plaut et al., 2007). m_{cap} is the MCID mass (presently 2.68×10^{16} kg; Putzig et al., 2018), $H = 11.1$ km is the scale height, a_{cap} is the area of the cap, and $\rho_{CO_2} = 1600$ kg m^{-3} is the density of CO_2 ice. We take a_{cap} to be a the mean cross-sectional area of the MCID, 8×10^{10} m^2 and z_{base} to be the elevation of the interface between the MCID and the SPLD, 4,000 m (as in Buhler et al., 2020). $P_{eq,cap}$ is determined by vapor pressure equilibrium between the atmosphere and the MCID, according to Hourdin et al. (1993) (units: Pa):

$$P_{eq,cap} = 100 \exp\left[\frac{\dfrac{1}{-T_{eq,cap}} + 0.00734}{0.000324}\right] \tag{2}$$

$T_{eq,cap}$ is the equilibrium temperature in K of the surface of the MCID set by energy balance between incoming absorbed insolation flux and outgoing emitted thermal flux:

$$T_{eq} = \left(\frac{S_{\theta_S,\tau}\left(1 - A_{CO_2}\right)}{\epsilon_{CO_2}\sigma_B}\right)^{\frac{1}{4}} \tag{3}$$

Here, σ_B is the Stefan-Boltzmann constant and ϵ_{CO_2} is the column-integrated emissivity over the MCID. We select $\epsilon_{CO_2} = 0.8$, a value consistent with the loose bounds placed by observation (Hayne et al., 2011), and the value for which our model (Buhler et al., 2020) and the Global Circulation Model of Guo et al. (2010) simultaneously reproduce the modern seasonal CO_2 cycle and the Residual South Polar Cap (RSPC). $S_{\theta_S,\tau}$ is the incident surface insolation onto the RSPC, which caps the MCID (Figure 1b) and determines solar energy input into the MCID via heat transfer. $S_{\theta_S,\tau}$ is calculated in 30 min time steps and includes atmospheric opacity using a delta-Eddington scheme, as in Buhler et al. (2020). The opacity τ over the MCID was set to the time-varying value of the mean Montabone et al. (2015) observations in Mars Years 27–33 from 87°S–90°S, −90°E–0°E (the region corresponding to the location of the MCID), converted from infrared to optical opacity by multiplying by a factor of 2.6, as Montabone et al. (2015) suggest. The instantaneous MCID albedo A_{CO_2} depends on the insolation angle (Paige & Ingersoll, 1985), according to Buhler et al. (2020):

$$A_{CO_2} = 0.532 + 0.511 \times \cos\left(\theta_S\right) \tag{4}$$

Here, θ_S is the insolation incidence angle from nadir. A_{CO_2} is calculated at every 30-min time step based upon the instantaneous insolation angle.

2.2. CO₂ Exchange Between the Atmosphere and the Regolith

The regolith reservoir is divided into a grid of latitude and depth (e.g., Fanale et al., 1982). The mass of adsorbed CO_2 dm_{reg} in each grid box is calculated based upon $P_{eq,0}$ and the temperature T as a function of depth z, according to Zent and Quinn (1995):

$$dm_{reg} = dV_{reg}a_S\delta P_{eq,0}^{\gamma}T\left(z\right)^{\beta} \tag{5}$$

Here, dV_{reg} is the regolith volume of a given grid box, a_S is the specific surface area of the regolith, and $\delta = 5.749 \times 10^1$, $\gamma = 0.2788$, and $\beta = -4.0711$ are values fit to empirical data (Zent & Quinn, 1995). The value of a_S, especially beneath the top few centimeters, is not well constrained by observation. Therefore,

we investigate a_S spanning a range from $1 \times 10^2 \mathrm{m^2\ kg^{-1}}$ (a conservative lower bound based upon terrestrial basalt measurements; e.g., Nielsen & Fisk, 2010) to $1 \times 10^5 \mathrm{m^2\ kg^{-1}}$ (a typical value for palagonite used in martian analogue studies; Zent & Quinn, 1995). The total mass of CO_2 adsorbed in the regolith m_{reg} is the integral over all dm_{reg} elements.

Temperature is calculated from a one-dimensional energy balance model that accounts for incoming absorbed insolation energy flux, outgoing emitted thermal energy flux, and the energy flux conducted to the subsurface:

$$S_{\theta_S}\left(1 - A_{reg}\right) - \epsilon \sigma_B T^4 + k_{reg}\frac{dT}{dz} = 0 \tag{6}$$

Here, ϵ is emissivity, A_{reg} is the regolith surface albedo, and k_{reg} is the regolith thermal conductivity. We use an explicit numerical one-dimensional scheme that solves the diffusion equation with temperature-independent thermal diffusivity at each time-step to model subsurface heat conduction:

$$\frac{dT}{dt} = \frac{k_{reg}}{\rho c_p}\frac{d^2 T}{dz^2} \tag{7}$$

Here, ρ is the regolith density and c_p is the regolith heat capacity. We use $c_p = 837\ \mathrm{J\ kg^{-1}\ K^{-1}}$ and $\rho = 2{,}000\ \mathrm{kg\ m^{-3}}$ (Fanale et al., 1982). The subsurface grid has spacing that enlarges exponentially with depth and the width of the grid spacing adaptively adjusts to the minimum spacing required for numerical stability depending on the run parameters. We perform runs across a broad range of k_{reg}, from $0.0837\ \mathrm{W\ m^{-1}\ K^{-1}}$ (the low k_{reg} runs of Fanale et al., 1982, which corresponds to a thermal inertia of ~300 SI, a typical value for Mars's surface [e.g., Mellon et al., 2000; Palluconi & Kieffer, 1981]) to $2\ \mathrm{W\ m^{-1}\ K^{-1}}$ (thermal conductivity of zero-porosity mafic rock; Robertson, 1988). Under Mars conditions, ρ and c_p vary by much less than an order of magnitude, while k_{reg} can vary by several orders of magnitude, so we only analyze the model's sensitivity to varying k_{reg}, while leaving ρ and c_p fixed, as is common practice (e.g., Neugebauer et al., 1971).

We also vary the regolith albedo A_{reg} from 0.1 to 0.3, consistent with typical observed regolith albedo (Kieffer et al., 1977). This range encompasses the range (0.2–0.3) in which the majority of the mean annual temperatures as a function of obliquity and latitude in our model lie within 5% of the temperatures calculated by Haberle et al. (2003), which uses a consortium albedo. We do not vary regolith emissivity ($\varepsilon_{reg} = 1.0$) because the mean annual temperature varies as $\varepsilon_{reg} / \left(1 - A_{reg}\right)$, and so varying ε_{reg} would be redundant with varying A_{reg}.

We calculate the temperature using Equation 7 in 30 min time steps down to a depth of 50 m (>10 annual skin depths), where the boundary condition is Mars' geothermal energy flux F_{geo}. Below a depth of 50 m the temperature is set according to $dT/dz = -F_{geo}/k_{reg}$. In our model, we use $F_{geo} = 0.03\ \mathrm{W\ m^{-2}}$ (Dehant et al., 2012; Schubert et al., 1992; Zuber et al., 2000). We do not vary F_{geo} because the temperature gradient depends on the ratio of F_{geo}/k_{reg}, and so varying F_{geo} would be redundant with varying k_{reg}.

The depth to which exchangeable CO_2 adsorbs onto the regolith z_{reg} is unknown from observation. We run our model across a range of z_{reg} from 1 m to 1 km, which encompasses the range of z_{reg} investigated by previous studies (Fanale et al., 1982; Zent & Quinn, 1995; see also discussion in Section 4.2). We use Equation 5 to calculate the current mass of CO_2 adsorbed in the regolith m_{reg} for each set of input parameters, given the current orbit and observed mean annual atmospheric pressure.

We note that Zent and Quinn (1995) find that water competes poorly for adsorption sites at the low pressures and temperatures characteristic of the Martian regolith. Thus, including H_2O adsorption has a negligible effect on global CO_2 adsorption, so we choose not to include it in our model. Including their estimated ~10% displacement of CO_2 adsorbate by H_2O as an independent uncertainty in quadrature with our formal uncertainty estimate yields a ~0.6 mbar increase of our reported upper bound and ~1.4 mbar decrease on the lower bound.

2.3. Coupled CO_2 Exchange Between the Atmosphere, MCID, and Regolith, and Stratigraphy

The total mass of Mars' exchangeable CO_2 on obliquity timescales is $m_{tot} = m_{atm} + m_{cap} + m_{reg}$, a conserved quantity in our model. In each model, the current m_{reg} is determined by calculating the total modern regolith adsorption based on current insolation, pressure, and MCID mass, which ensures that each model reproduces current observations of Mars' CO_2 distribution. We model how m_{tot} partitions between m_{atm}, m_{cap}, and m_{reg} across a grid of obliquities (0°–90° in 5° steps and at 25.2°, 26.7°, 30.5°, and 33.8°, which are the current obliquity and the most recent three obliquity maxima (Laskar et al., 2004) and regolith properties (z_{reg}, a_S, A_{reg}, and k_{reg}, as described in Section 2.2). At each grid point, we iteratively compute atmosphere-MCID and atmosphere-regolith equilibria, until the mass of each reservoir is within 0.1% of the mass from the previous iteration (typically <5 iterations), as consistent with our model framework of insignificant kinetic hindrance to CO_2 exchange on obliquity timescales. We then interpolate between grid points to find the mass of each reservoir for any desired set of parameters.

Model-predicted stratigraphy is determined as described in Buhler et al. (2020). In short, the model outputs a synthetic MCID stratigraphy composed of alternating layers of CO_2 and H_2O ice. As Mars' orbit cycles, CO_2 accumulates onto and ablates from the top of the MCID. When CO_2 ablates, H_2O lag concentrates into a layer atop the MCID. Lag layers are buried when CO_2 is subsequently deposited. The mass of CO_2 between two H_2O layers is thus the difference in CO_2 ice mass during adjacent monotonic minima in MCID CO_2 mass; lag layers formed at nonmonotonic minima are subsumed into lag layers formed at later, more extreme minima (see Figure 3 of Buhler et al., 2020). We only report mass values for CO_2 layers, not H_2O layers (nb., modeled H_2O layer thicknesses would be the same as reported in Buhler et al., 2020 for all model runs). That is, we treat H_2O layers as marker beds; their thickness is not important for our approach to determining Mars' CO_2 exchange cycle or total CO_2 mass inventory.

2.4. Best-Fit Parameter Determination

Each suite of parameters yields a synthetic model-predicted MCID stratigraphy. We compare the mass ratio of CO_2 layers in synthetic MCID stratigraphic columns to the observed mass ratio of CO_2 layers based upon the data reported by Bierson et al. (2016) (Figure 1). We determine the masses of each of the layers by multiplying the mean layer thicknesses (Table 1 of Bierson et al., 2016) by the area of the corresponding bounding layer capping each layer (Figure 1b of Bierson et al., 2016). We obtain masses of 77%, 21%, and 2% of the total MCID mass for the top (AA$_{3c}$), middle (AA$_{3b}$), and bottom (AA$_{3a}$) layers, respectively (Figure 1b); these values are consistent with the most recent efforts to measure the individual layer masses (Alwarda & Smith, 2019).

Bierson et al. (2016) do not report errors on their measurements, so we assign an observation uncertainty according to the following procedure. We account for two sources of observational uncertainty. First, the difference between the total MCID masses derived by Bierson et al. (2016) and Putzig et al. (2018) is 11%, which we conservatively take to be the 1σ measurement uncertainty for the entire MCID. Because there are three layers, we take one-third of the difference (3.3% the mass of the entire MCID) to be the 1σ measurement uncertainty for each layer. Second, 48% of the reported total MCID mass is extrapolated by surface geologic mapping (Bierson et al., 2016; Putzig et al., 2018). We conservatively estimate that the total extrapolated MCID mass is the 3σ uncertainty on the mass of each layer; that is, extrapolation yields a 1σ error of 16% of the entire MCID mass for each layer. These sources of error are independent, so we add them in quadrature to obtain a 1σ uncertainty of $\sigma_{obs} = 16.3\%$ the mass of the total MCID (4.36×10^{15} kg) for each layer. Selecting a different uncertainty value does not change the peak of the best-fit parameter determination, only the spread. We conducted a Markov Chain Monte Carlo (MCMC) simulation with 1×10^7 steps covering the full range of A_{reg}, k_{reg}, z_{reg}, and A_s as described above. The χ^2 value evaluated at each MCMC step was:

$$\chi^2 = \sum_{n=1}^{n=4} \left(\frac{m_{n,syn} - m_{n,obs}}{\sigma_{obs}} \right)^2 \qquad (8)$$
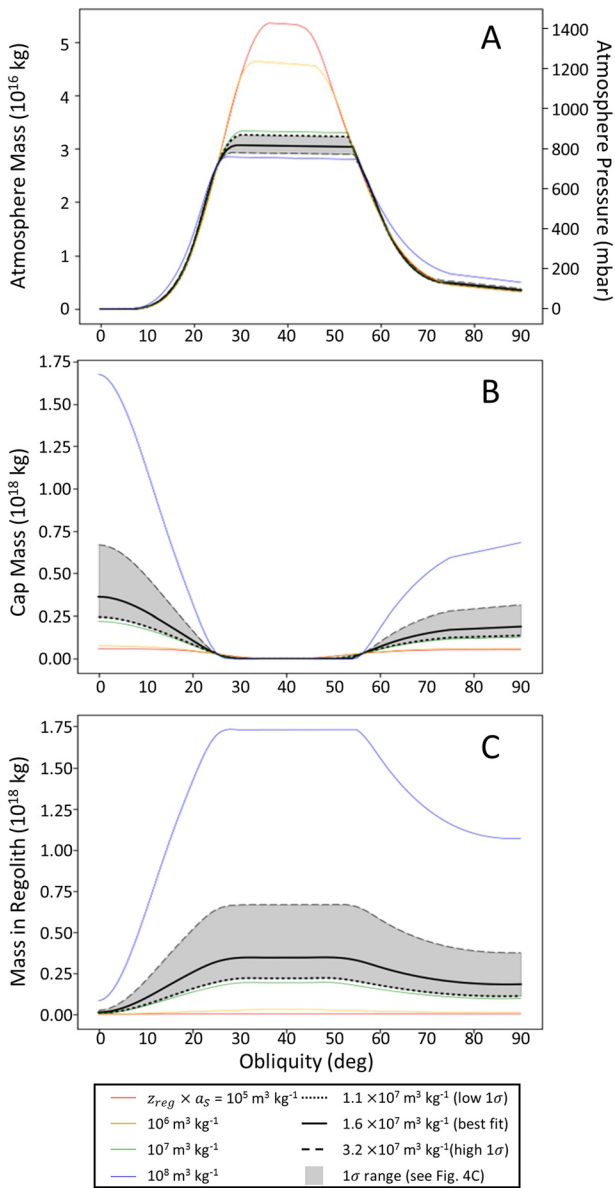
Figure 3. The mass in each reservoir ((a) Atmosphere, (b) Cap, (c) Regolith) as a function of obliquity for various values of regolith adsorptive capacity ($z_{reg} \times a_S$). Note significant divergence in model-predicted atmospheric mass as a function of z_{reg} in the range $\varepsilon \approx (30°, 55°)$ in panel (a).

Here, n is the layer number, $m_{n,\text{syn}}$ is the synthetic layer mass determined from the parameters called for a given MCMC step, and $m_{n,\text{obs}}$ is the observed layer mass. The results of the MCMC yield the model parameters that produce synthetic MCID stratigraphic columns that best agree with observation, with quantified uncertainty. We then used the parameter probability distribution obtained from the MCMC to calculate the predicted best-fit and uncertainty in regolith adsorptive capacity, m_{tot} and m_{reg}.

3. Results

3.1. Mass Exchange Between CO_2 Reservoirs as a Function of Obliquity

We use our model to calculate the mass in each CO_2 reservoir (atmosphere, regolith, and MCID) as a function of obliquity. Figure 3 shows the CO_2 mass in each reservoir for various values of regolith adsorptive capacity (the product of regolith thickness z_{reg} and specific surface area a_S): 10^5, 10^6, 10^7, and 10^8 m^3 kg^{-1}.

3.1.1. MCID CO_2 Mass as a Function of Obliquity

At low obliquity, the poles receive low insolation, leading to CO_2 ice deposition and a larger MCID mass (Figure 3b). As obliquity increases, the poles receive more sunlight and CO_2 sublimes from the pole, decreasing the MCID mass. Under our assumed insolation-dependent A_{CO_2} (Equation 4), when ε increases above ~40°, the amount of absorbed insolation by the polar CO_2 ice begins to decrease because the reflected insolation increases at a greater rate than the incident insolation (see Buhler et al., 2020; their supplementary figure 4). Thus the stability of polar CO_2 ice increases as a function of obliquity when $\varepsilon > \sim 40°$ (see further discussion in Section 4.5).

For the observed elevation of the base of the MCID, our model predicts that polar CO_2 ice is present at all obliquities if there is no regolith adsorption. As regolith adsorptive capacity increases, the magnitude of CO_2 fluxing onto and off of the MCID increases simply because there is more CO_2 in the system (Figure 3). Thus, when the regolith adsorptive capacity is larger, the mass of the MCID is proportionately larger when the MCID experiences low absorbed insolation ($\varepsilon < 25°$ or $\varepsilon > 55°$) and proportionately smaller when the MCID experiences high absorbed insolation ($\varepsilon \sim 25°–55°$).

3.1.2. Regolith CO_2 Mass as a Function of Obliquity

Under Mars conditions, the regolith-atmosphere equilibrium pressure typically lies above the MCID-atmosphere equilibrium pressure, unless the regolith adsorptive capacity is sufficiently large and the obliquity is moderate (e.g., $\varepsilon \sim 30°–50°$; Figure 3b). Thus, the system typically adjusts to a state with the atmospheric pressure set by MCID-atmosphere vapor pressure equilibration via deposition of polar CO_2 ice, with only passive adjustment of CO_2 regolith adsorption.

However, when the regolith adsorptive capacity is sufficiently large, the mass of adsorbed CO_2 required to equilibrate with the atmosphere becomes substantial compared to the entire exchangeable CO_2 inventory. Additionally, at moderate obliquities, the MCID-atmosphere equilibrium pressure is particularly high because the MCID is near maximum insolation absorption. When these effects combine, the regolith-atmosphere equilibrium pressure can fall below the MCID-atmosphere equilibrium pressure, making polar CO_2 ice energetically disfavored compared to adsorption of CO_2 in the regolith. For this reason, nonzero

Table 1
Maximum Atmospheric Pressure as a Function of Regolith Adsorptive Capacity (Product of z_{reg} and a_S)

Adsorptive capacity (m^3 kg^{-1})	Maximum $P_{eq,0}$ (Pa)
0*	1,430
10^5	1,400
10^6	1,160
10^7	910
1.1×10^7	900
1.6×10^7	840
3.2×10^7	780
10^8	760

*0 m value from Buhler et al. (2020)

regolith adsorptive capacity causes the MCID to disappear in an obliquity range centered at approximately $\varepsilon \approx 40°$ (Figure 3b). Additionally, when polar CO_2 is no longer stable, the atmospheric pressure drops below the MCID-atmosphere equilibrium pressure (Figure 3a), and the regolith and atmospheric mass curves flatten as a function of obliquity (following the power-law relation of Equation 5, rather than the exponential relation of Equation 2; Figure 3c). The range of obliquity for which the MCID disappears increases for increasing regolith adsorptive capacity (Figure 3b).

3.1.3. Atmospheric CO_2 Mass as a Function of Obliquity

Under Mars conditions, vapor pressure equilibrium between the atmosphere and the MCID controls the atmospheric mass unless the MCID disappears. Thus, the atmospheric pressure as a function of obliquity mostly follows the MCID-atmosphere equilibrium line (Figure 3a). However, Figure 3a also reveals small differences in the atmospheric mass curves for different regolith adsorptive capacity across all ε. These small differences are due to the difference in MCID mass as a function of obliquity for model runs with differing regolith adsorptive capacity. When the MCID mass is larger, the thickness of the MCID is greater and equilibration between the atmosphere and the MCID occurs at a higher elevation, so the zero-elevation pressure is higher (Equation 1).

When the MCID does disappear, there is significant divergence in model-predicted atmospheric mass as a function of regolith adsorptive capacity in the range $\varepsilon \approx 30°–50°$ (Figure 3a). Because this divergence occurs near maximum atmospheric pressure, models with larger regolith adsorptive capacity experience smaller maximum surface pressure (e.g., ~40% lower for an adsorptive capacity of 10^8 m^3 kg^{-1} than an adsorptive capacity of 10^5 m^3 kg^{-1}; Table 1).

3.2. Best-Fit Parameters

The marginalized probability densities for z_{reg}, a_S, regolith adsorptive capacity (the product of z_{reg} and a_S), and joint z_{reg} and a_S distribution from the MCMC simulation are shown in Figure 4. Neither z_{reg} nor a_S individually has a strong peak, although values of $z_{reg} < {\sim}200$ m and $a_S < {\sim}2 \times 10^4$ m^2 kg^{-1} are disfavored. However, the regolith adsorptive capacity does have a clear peak and confidence interval of $1.6^{+2.2}_{-0.5} \times 10^7$ m^3 kg^{-1} (Figure 4c). The joint z_{reg} and a_S probability distribution shows that the model preference for z_{reg} and a_S are inversely proportional, yielding a clear constraint on regolith adsorptive capacity despite no strong preference for z_{reg} or a_S individually (Figure 4d). A_{reg} and k_{reg} each have a uniform probability distribution and so are not shown.

For each step in the MCMC chain, we calculated the total CO_2 inventory corresponding to the parameters in that step in order to find the probability distribution of Mars' obliquity-timescale exchangeable CO_2 inventory m_{tot}, based upon our model results (Figure 5). The maximum likelihood value and 68% confidence interval for m_{tot} is $3.8^{+3.0}_{-1.3} \times 10^{17}$ kg (100^{+80}_{-34} mbar).

3.3. Historical Evolution of Mars' CO_2 Reservoirs and Its Effect on MCID Stratigraphy

The model-predicted historical 1 Myr mass evolution of the MCID, regolith, and atmosphere CO_2 reservoirs is shown for various values of regolith adsorptive capacity in Figure 6. In general, the m_{atm} history is similar in all models, except during epochs near maximum pressure when the MCID completely ablates, as discussed in Section 3.1.3 (Figure 3a; Table 1). In contrast, the m_{reg} history strongly depends on the regolith adsorptive capacity. Although the proportional variation in m_{reg} is similar across all models, the absolute magnitude of variation in m_{reg} is much larger in models with large m_{reg} (Figure 6d). For example, the variation of m_{reg} is ~1% that of m_{atm} when the regolith adsorptive capacity is 10^5 m^3 kg^{-1}, but ~500% that of m_{atm} when the regolith adsorptive capacity is 10^8 m^3 kg^{-1}. Thus, m_{cap} evolves complementarily to the evolution of m_{atm} when $m_{atm} >> m_{reg}$, but complementarily to m_{reg} when $m_{reg} >> m_{atm}$, with an intermediate evolution when $m_{reg} \approx m_{atm}$ (Figure 6). Because the rate of change with obliquity of the m_{atm} and m_{reg} histories are
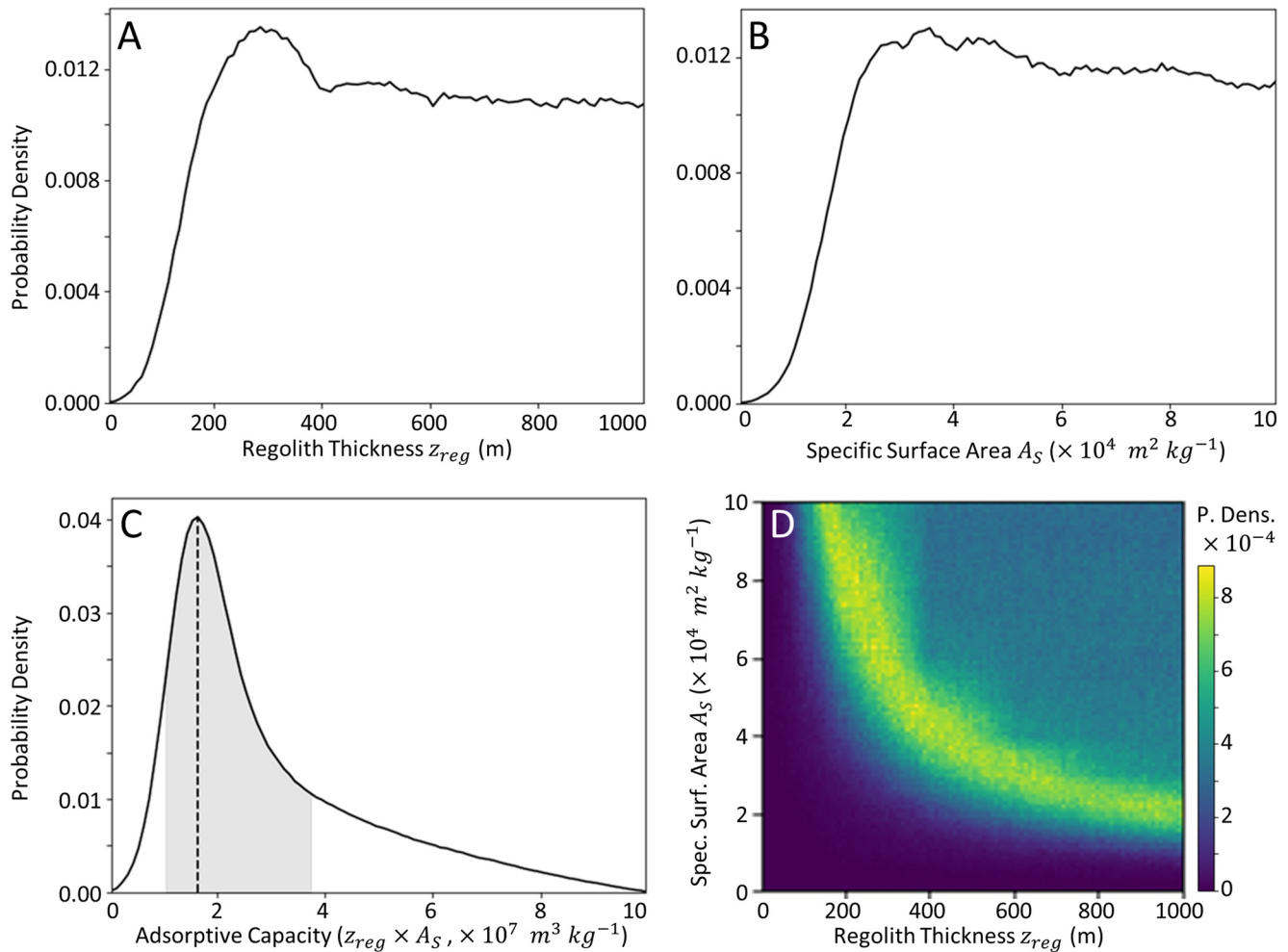
Figure 4. Marginalized probability of (a) z_{reg} and (b) a_S from the Markov Chain Monte Carlo (MCMC) comparison between model-output massive CO_2 ice deposit (MCID) stratigraphy and observed MCID stratigraphy. The surface albedo and thermal conductivity probability distributions are uniform not shown. (c) Probability distribution of regolith adsorptive capacity ($z_{reg} \times a_S$). Shaded region is 68% confidence interval. Vertical dashed line marks value of maximum probability. (d) Joint probability distribution of z_{reg} and a_S with color bar indicating probability density.

different, the proportional difference in local extrema in the historical evolution of m_{cap} depends upon the regolith adsorptive capacity. Thus, the proportional mass of CO_2 layers between H_2O bounding layers in the MCID stratigraphic column depends on the regolith adsorptive capacity because the mass of each CO_2 layer between demarcating H_2O layers depends on the difference between adjacent monotonic local m_{cap} minima (Buhler et al., 2020).

In particular, models with larger regolith adsorptive capacity yield predicted MCID stratigraphic columns with relatively thicker upper CO_2 layers and relatively thinner lower CO_2 layers (Figure 7). The lower layers are thinner because the variation in m_{cap} extrema are larger when regolith adsorptive capacity is larger, meaning that proportionally less CO_2 survived the more extreme, older minima in m_{cap} (i.e., the 97 and 385 kyr minima; Figure 6c). Likewise, the upper layers are thicker because more CO_2 fluxes back onto the cap during the recent lower obliquity periods (Figure 6c).

3.4. Relative Importance of Parameters for Determining MCID Stratigraphy

The regolith adsorptive capacity (product of a_S and k_{reg}) is the most important model parameter for determining model-predicted MCID stratigraphy, more important than the particular values of z_{reg} or a_S (Figure 4). a_S and z_{reg} each have a slightly different effect on regolith adsorptive capacity. a_S has a linear effect on
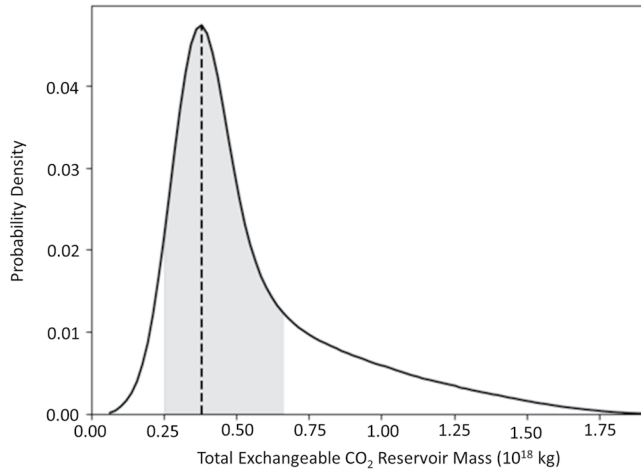
Figure 5. Probability of Mars' total mobile CO_2 inventory calculated from the output chain of the Markov Chain Monte Carlo (MCMC) comparison between model-output massive CO_2 ice deposit (MCID) stratigraphy and observed MCID stratigraphy. Shaded region is 68% confidence interval. Vertical dashed line marks value of maximum probability.

the regolith adsorptive capacity (Equation 5). In the shallow subsurface, increasing z_{reg} also approximately linearly increases the regolith adsorptive capacity. However, going deeper, regolith temperature increases with depth, leading to diminishing returns for regolith adsorptive capacity with increasing depth because of the inverse ~fourth power dependence of adsorption on temperature (Equation 5). That is, deeper regolith is less effective at adsorbing CO_2 because it is warmer. The exact decrease in adsorptive capacity with depth depends on k_{reg}; larger k_{reg} results in a more gradual temperature increase with depth. The adsorptive capacity of regolith at 1 km depth typically is ~(1, 10, 50, 70)% that of regolith in the top few meters for $k_{reg} = (0.0837, 0.25, 1.0, 2.0)$ W m^{-1} K^{-1}, respectively for the low-to-mid-latitudes at present obliquity.

Varying the regolith adsorptive capacity (product of z_{reg} and a_S) has a stronger effect on the model-predicted MCID stratigraphic column than does varying k_{reg}. The reason is because the 1σ range of the regolith adsorptive capacity varies across a range of 3.5×10^7 m^3 kg^{-1}. In comparison, the maximum difference in $T(z)^\beta$ between $\varepsilon = 25.2°$ and $30.5°$ for each regolith chunk across the entire range of plausible k_{reg} (0.0837–2.0 W m^{-1} K^{-1}) is only 3×10^4. Thus, in the parameter space relevant to Mars, the plausible range of regolith adsorptive capacity is approximately three orders of magnitude more important for determining m_{reg} variations between $\varepsilon = 25.2°$ and $30.5°$ than is the plausible range of k_{reg} (Equation 5). The variations in m_{reg}, in turn, affect the variations in m_{cap} and the model-predicted stratigraphy (Section 3.3). The relevant range of A_{reg} (0.1–0.3) has an even smaller effect than k_{reg} on $T(z)^\beta$ differences (and thus m_{reg} and m_{cap} differences) between obliquities and so is even less important for determining the model-predicted MCID stratigraphy.
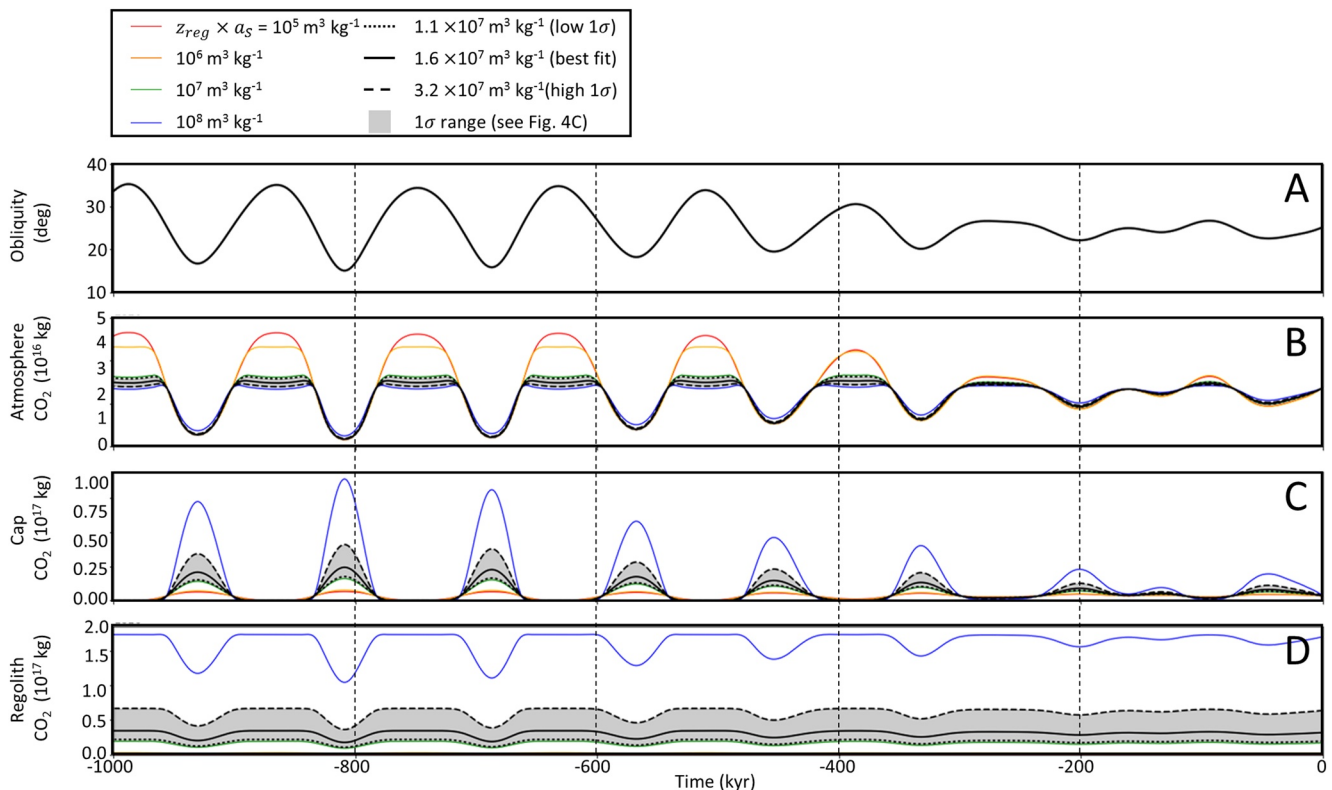

Figure 6. Model history of Mars' CO_2 reservoirs for various values of regolith adsorptive capacity ($z_{reg} \times a_S$). (a) Obliquity history of Mars (Laskar et al., 2004). (b) Mass of CO_2 in the atmosphere. (c) Mass of massive CO_2 ice deposit (MCID). (d) Mass of CO_2 adsorbed in regolith. Legend colors as in Figure 3.
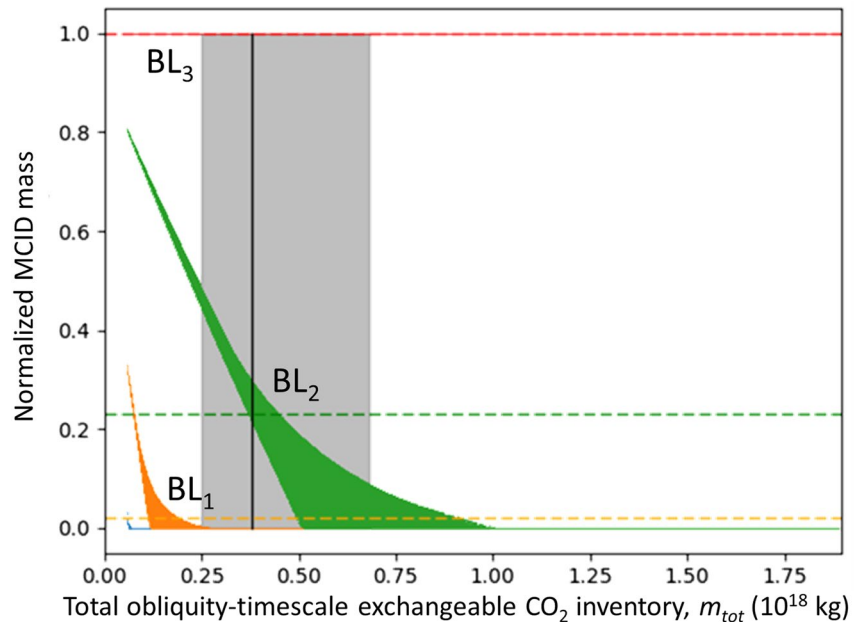
Figure 7. Location of H_2O ice bounding layers (BL) in the stratigraphic column relative to normalized massive CO_2 ice deposit (MCID) mass from model runs (compare to observed stratigraphy in Figure 1B). Colored areas (red = BL_3, green = BL_2, yellow = BL_1, blue = additional, unobserved BL) indicate the range of model-predicted BL elevations as a function of model m_{tot}. Dashed lines of corresponding color indicate observed BL elevations. Vertical black line and gray region indicate best-fit and 1σ range on m_{tot} from Markov Chain Monte Carlo (MCMC) model. Modeled BL locations in the stratigraphy cover a range of values for a particular m_{tot} because different combinations of z_{reg}, a_S, and k_{reg} can yield the same m_{tot} but different stratigraphic output. Increasing m_{tot} yields models with more massive upper CO_2 layers (BLs lower in the stratigraphic column). Models with $m_{tot} > \sim 1 \times 10^{18}$ kg have only a single BL at the top of the MCID. Total present-day MCID CO_2 mass (2.68×10^{16} kg) is the same for all models, regardless of m_{tot}.

4. Discussion

4.1. Preferred Parameter Values

Our model indicates that regolith with an adsorptive capacity ($a_S \times z_{reg}$) of $1.6^{+2.2}_{-0.5} \times 10^7 \ m^3 \ kg^{-1}$ on obliquity timescales, regardless of k_{reg} and A_{reg}, yields a model stratigraphy that is most consistent with observation (Figures 4c and 7). This adsorptive capacity implies that the current reservoir of adsorbed CO_2 that can exchange on obliquity timescales is $3.2^{+3.0}_{-1.2} \times 10^{17}$ kg (86^{+80}_{-34} mbar, 68% confidence interval; Figures 5 and 7). Combined with observational estimates of the mass of the present atmosphere (2.8×10^{16} kg; Haberle et al., 2008; Guo et al., 2010) and the MCID (2.7×10^{16} kg; Putzig et al., 2018), our study indicates that the total reservoir of CO_2 that exchanges on obliquity timescales is $3.8^{+3.0}_{-1.2} \times 10^{17}$ kg (100^{+80}_{-34} mbar, 68% confidence interval; Figure 5).

4.2. Geologic Interpretation

Mars's crustal thermal and physical properties are horizontally and vertically variable with a wide range of induration and micro/macroscopic properties (Bandfield et al., 2013). However, thermal conductivity and geomorphic observations provide some insight into the near-surface crustal structure. Competent basaltic bedrock is associated with high thermal conductivities of ≥ 2 W m^{-1} K^{-1} (e.g., Clauser & Huenges, 1995; Robertson, 1988) and inertias of $>1,200$ J $m^{-2}K^{-1}s^{-1/2}$ (Edwards et al., 2009). Such high values are frequently detected on the Martian surface from orbit, although covering only a small fraction ($\sim 1\%$) of the surface (Edwards et al., 2008, 2014; Rogers et al., 2018). The most common surface layer thermal conductivity derived on Mars from thermal infrared observations is ~ 0.04 W m^{-1} K^{-1}, suggestive of loose sand-like material (Kieffer, 2013). Analysis of high-resolution imagery of cliffs (Golombek et al, 2017, 2018; Warner

et al., 2017) as well as small crater ejecta material properties (Golombek et al., 2020) indicates that the loose surficial layer may typically be only a few meters thick, on top of competent and sometimes jointed bedrock.

Our results are consistent with CO_2 adsorption occurring in a several-hundred-meter to ~kilometer-thick layer with a_S in the range of a few $\times 10^4$–~10^5 m^2 kg^{-1}. However, the key point is that the model predicts an MCID stratigraphy most consistent with observation when the regolith adsorptive capacity, the product of a_S and z_{reg}, is $1.6^{+2.2}_{-0.5} \times 10^7$ m^3 kg^{-1} on obliquity timescales (Figures 4c and 4d); the individual values of a_S and z_{reg} are not tightly constrained by the model.

The value of a_S at the surface of Mars where Viking 1 landed has a lower bound constraint from *in situ* measurements of ~1×10^3 m^2 kg^{-1} (Ballou et al., 1978). The model preference for $a_S >$~2×10^4 m^2 kg^{-1} is consistent with this observation (Figure 4b) and with laboratory measurements of a_S for terrestrial rocks, which range from ~1×10^2 to ~1×10^5 m^2 kg^{-1} (Nielsen & Fisk, 2010; Zent & Quinn, 1995; and references therein).

Measurements from the InSight lander indicate that ductile-creep mediated porosity closure may occur at ~8–11 km at the InSight landing location (Gyalay et al., 2020; Lognonne et al., 2020). However, the depth to which the majority of the adsorptive exchange of CO_2 occurs on obliquity timescales is likely confined to <~1 km because of (1) decreasing porosity with depth, (2) increasing temperature with depth, and (3) thermal wave decay with depth.

At depths shallower than the depth of ductile-creep closure, Mars' regolith likely experiences elastic pore closure with a characteristic exponential decay in porosity of ~3 km (Clifford, 1993), based on a scaling from a model lunar relationship (Binder & Lange, 1980) and analogy to terrestrial observations (Athy, 1930; Schmoker & Gautier, 1988). Second, the regolith adsorptive capacity decays with depth by a factor of ~0.01–~0.7 per km for k_{reg} = 0.0837 or 2.0 W m^{-1} K^{-1}, respectively because the regolith is warmer (Section 3.4). Third, temperature variations as a function of obliquity oscillations, which drive changes in m_{reg}, damp exponentially with a thermal skin depth of ~220–~1,000 m for k_{reg} = 0.0837 and 2.0 W m^{-1} K^{-1}, respectively. Taken together, the effective contribution of a particular regolith chunk to changes in m_{reg} as a function of obliquity decays by a factor of ~6–~>10,000 per km for k_{reg} = 2.0 and k_{reg} = 0.0837 W m^{-1} K^{-1}, respectively. That is, ~85%–>>99% of CO_2 exchange on obliquity cycles is expected to take place in regolith shallower than 1 km depth. Comparatively, for pore sizes of 1–20 microns (consistent with literature estimates; e.g., Clifford, 1991; Morgan et al., 2018; Toon et al., 1980), the 10^5-year vapor diffusion e-folding skin depth is ~1.5–7 km (see Equation 7 of Toon et al., 1980). Thus, the influence of thermal and surface area availability controls on regolith adsorption are likely moderately to substantially more important for setting the depth-scale of regolith adsorption than vapor diffusion, consistent with the conclusions of Toon et al. (1980). Accordingly, we estimate that obliquity-timescale CO_2 adsorptive exchange occurs within a regolith reservoir of depth <~1 km (as just discussed) to >~200 m (Figure 4a) with a corresponding a_S such that the regolith adsorptive capacity is in the range $1.6^{+2.2}_{-0.5} \times 10^7$ m^3 kg^{-1} (Figure 4c).

4.3. Comparison to Other Estimates of Mars' Exchangeable CO_2 Inventory

Zent and Quinn (1995) explored models with a range of regolith thickness from 1 to 1,000 m. They preferred a model with a regolith thickness of 75 m, but were unable to distinguish a preferred value of Mars' total CO_2 inventory based on a comparison between their model predictions and observation of the polar CO_2 ice deposit alone. Thus, they preferred an obliquity-timescale exchangeable CO_2 inventory of 26.8 mbar, but obtained model outputs with equivalently good fits to then-available polar CO_2 ice observations for total CO_2 inventories spanning 7.4–187 mbar. Similarly, Fanale et al. (1982) ran models assuming various regolith adsorption curves (cf. Equation 5) and regolith thicknesses ranging from 100 to 1,000 m and obtained a range of obliquity-timescale exchangeable CO_2 reservoirs ranging from 62.5 to 500 mbar with equal probability, based solely on comparing their model results to then-available polar CO_2 ice observations.

Compared to previous attempts, the key benefit of our estimate is our comparison of model results with the CO_2 record stored in the MCID. Because of these new observations, our model results are fit to more accurate observations of Mars' present-day CO_2 inventory. We also obtain internally consistent derivation of

the total adsorptive capacity of Mars' regolith with quantified uncertainty rather than relying on selecting a preferred regolith adsorptive capacity as input to the model.

4.4. Application to Amazonian Climate Modeling

The peak mean annual pressure experienced by Mars is ~40% lower when our model includes an adsorbing regolith with the best-fit regolith adsorptive capacity (3.1×10^{16} kg; Figure 3a) than our model without adsorbing regolith (5.4×10^{16} kg; Buhler et al., 2020). A 40% pressure reduction may have significant implications for climate investigations, such as studies of the stability of liquid surface water and (near-) surface habitability of Mars (e.g., Ingersoll, 1970; Richardson & Mischna, 2005). Therefore, we provide our model m_{atm}, m_{reg}, and m_{cap} solutions as a function of obliquity ε (0°–90° in 1° increments) and regolith adsorptive capacity (10^5, 10^6, 10^7, 1.1×10^7, 1.6×10^7, 3.2×10^7, and 10^8 m^3 kg^{-1}), in a public repository (Buhler and Piqueux, 2021) in order to aid climate studies. We note that the total flux of CO_2 loss to space every 20 Myr is ~1% the best-fit flux of CO_2 exchanging between the atmosphere, regolith, and cap during a typical obliquity cycle (Jakosky et al., 2018). Therefore, the appended tables are most relevant to climate studies targeting the past few hundred Myr.

4.5. Further Discussion and Future Work

In order to focus the scope of this investigation to the goals of elucidating the basic mechanisms by which Mars' adsorbed CO_2 reservoir affects the stratigraphic record of the MCID, we have focused on how varying regolith-specific parameters affects the MCID stratigraphy. Varying MCID properties (e.g., basal elevation of the MCID, the CO_2 albedo and emissivity, MCID area, atmospheric opacity over the cap, and slopes) will also affect the MCID stratigraphy, but are outside the scope of this study and saved for future work.

In particular, for this study, we elect to present results using a single observation-based insolation-dependent albedo function (Equation 4, Paige & Ingersoll, 1985) that represents the aggregate albedo properties of the surface south polar CO_2 ice in the present climate. These optical properties are thought to arise due to the style (ratio of snowfall to direct deposition) of wintertime CO_2 deposition over the RSPC set by global topographic forcing (Colaprete et al., 2005). CO_2 deposition annually renews the upper surface of the RSPC and preserves the bright albedo properties of the RSPC (Buhler et al., 2017; Thomas et al., 2016). Although published climate studies have not yet focused specifically on seasonally resolved deposition of CO_2 onto the south polar cap as a function of obliquity, modeling indicates that Mars' general climatic behavior over the range of 25°–35° obliquity is grossly comparable to the present (e.g., Madeleine et al., 2009). The present-day stratigraphy of the MCID depends on the climatic behavior between 25.2° (present) and 30.5° obliquity (the penultimate monotonic obliquity maximum), which lies conservatively in this range. Moreover, no predictions exist in the literature for how CO_2 albedo dependence on insolation might vary with obliquity. Thus, we elect to use a single albedo function based upon present-day observations (Equation 4), rather than exploring arbitrary variations to the coefficients in the albedo function for the full MCMC analysis.

As with any modeling effort, extrapolating the results of our study to climatic and orbit conditions substantially different from the present day warrants caution. In particular, use of the Equation 4 albedo function yields a model prediction that a polar CO_2 cap reappears for obliquities >~55° using best-fit model parameters (Section 3.1.1). To test the qualitative robustness of this prediction, we performed a sensitivity study in which we covaried the coefficients for the constant and insolation-dependent terms in Equation 4, with the constraint that the mean annual albedo of the present obliquity matches observation. We found that absorbed insolation by polar CO_2 ice inflects (begins to decrease with higher obliquity) for all values of the insolation-dependent coefficient above 0.24; in particular, the inflection lies between 25° and 55° obliquity for all values of the insolation-dependent coefficient between ~0.3 and ~0.8 (half of the total physically meaningful range). The observed value of the insolation-dependent coefficient is 0.511 (Equation 4), with an absorbed insolation inflection at ~40° obliquity (Section 3.1.1), so these results indicate that the prediction is robust against variation to the albedo function. However, gross changes in other processes that are not assessed in our model, such as dust lofting, cloud distributions, other climatic factors, etc., may affect whether a polar CO_2 cap is actually stable at high obliquities. The deposition and ablation of large seasonal caps at high obliquities may also cause disequilibrium between the regolith and cap reservoirs.

Additionally, at high obliquities ($>\sim60°$), equatorial regions receive less annually averaged incident insolation than the poles, which could conceivably lead to perennial low-latitude CO_2 deposits (cf., midlatitude and equatorial water ice deposits; e.g., Head et al., 2003, 2005; Holt et al., 2008). The relative stability of perennial CO_2 deposits depends on a combination of physical dependencies (Section 2.1). For example, south polar CO_2 is evidently more stable than north polar CO_2 because south polar CO_2 has higher albedo and emissivity, even though it resides at higher elevation (Buhler et al., 2020). There are, however, sparse deposits near 70°N interpreted as moraines from CO_2 glaciers forming at very low obliquities (Kreslavsky & Head, 2011), indicating that nonsouth-polar perennial CO_2 deposits may be possible under some conditions. However, because the latitude, elevation, and optical properties of putative high-obliquity nonpolar CO_2 deposits are unknown, assessment of their formation is not presently possible. Nevertheless, this discussion of potential high-obliquity behavior of perennial CO_2 deposition does not change our conclusions about the formation of the presently observed MCID nor our quantitative derivation of the obliquity-timescale mobile CO_2 inventory.

We also note that we have used a one-dimensional model of MCID stratigraphic development that does not account for lateral stratigraphic variation. Quantified results of the laterally varying thickness of individual CO_2 ice layers in the MCID are not yet available, but are hopefully forthcoming (Alwarda & Smith, 2019). More observational study of the MCID to quantify lateral thickness variation of layers, uncertainty in layer thicknesses, and mass and structure of the portion of the MCID in the observational gore poleward of $\sim87.5°S$ (e.g., Putzig et al., 2018) will improve our understanding of Mars' mobile CO_2 inventory. Finally, other effects, such as viscous relaxation of CO_2 ice in the MCID (Smith et al., 2021), may affect the stratigraphic evolution of the MCID. However, it is not yet clear exactly how these effects may manifest. For example, viscous flow may lead to thicker bottom layers (due to ponding in topographic lows) or thinner bottom layers (due to lateral spreading), or these effects might average out over the entire extent of the MCID.

Nevertheless, we have used a representative set of MCID properties based on observation and our model predicts stratigraphic columns that are similar to the observed MCID stratigraphy. Thus, we are confident that our estimate of Mars' exchangeable CO_2 inventory significantly improves on previous estimates that were made before the discovery of the MCID.

5. Conclusion

We used a numerical simulation to model the exchange between Mars' three mobile CO_2 reservoirs, CO_2 adsorbed in the regolith, the atmosphere, and the MCID, in order to obtain predicted stratigraphic columns of the MCID. We then compared the model-predicted MCID stratigraphy to the observed stratigraphy in order to obtain a best-fit estimate for Mars' obliquity-timescale regolith adsorptive capacity (the product of active regolith thickness and specific surface area), $1.6^{+2.2}_{-0.5} \times 10^7 \, \mathrm{m^3 \, kg^{-1}}$ (68% confidence), and total CO_2 inventory that is mobile on obliquity timescales, $3.8^{+3.0}_{-1.3} \times 10^{17}$ kg (100^{+80}_{-34} mbar; 68% confidence). Adsorptive CO_2 exchange with the regolith on obliquity timescales likely occurs in the depth range of $<\sim200$ m$->\sim1$ km, with the deeper bound set by thermal processes and adsorptive surface availability. We find that the regolith surface albedo and thermal conductivity play a negligible role in determining the stratigraphy predicted by our model.

The crucial advantage our estimate has over previous attempts is the benefit of comparing our model results to the record of CO_2 exchange stored in the MCID. Because of these new observations, our model results are fit to more accurate observations of Mars' present-day CO_2 inventory. We also obtain internally consistent derivation of the total adsorptive capacity of Mars' regolith with quantified uncertainty, rather than relying on selecting a preferred regolith adsorptive capacity as input to the model.

We used our model to reconstruct Mars' atmospheric pressure history over the past 1 Myr. We find that Mars' peak mean annual pressure is $\sim40\%$ lower when our model includes an adsorbing regolith with our preferred adsorptive capacity than our model without adsorbing regolith. The mass of Mars' exchangeable CO_2 reservoir and recent pressure history will be important for understanding the long-term evolution of Mars' climate, the pressure range experienced by Amazonian Mars, and the attendant implications for its near-surface habitability. We have provided machine-readable data tables with our results in Buhler and Piqueux (2021) to enhance future climate studies of Amazonian Mars.

Appendix A: Nomenclature

Table A1
Nomenclature

Symbol	Description	Value or prior range	Units
A_{CO_2}	Polar CO_2 ice albedo	Variable	Unitless
A_{reg}	**Regolith surface albedo**	**0.1–0.3**	**Unitless**
a_{cap}	Mean cross-sectional area of the polar CO_2 ice cap	8×10^{10}	m^2
a_S	**Specific surface area of the regolith**	**10^2–10^5**	**$m^2\,kg^{-1}$**
β	Empirical fit to CO_2 adsorption temperature power dependence from Zent and Quinn (1995)	-4.0711	Unitless
c_p	Regolith heat capacity	2,000	$J\,kg^{-1}\,K^{-1}$
γ	Empirical fit to CO_2 adsorption pressure power dependence from Zent and Quinn (1995)	0.2788	Unitless
dm_{reg}	Mass of adsorbed CO_2 in each grid box	Variable	kg
dV_{reg}	Regolith volume of a given grid box	Variable	m^3
δ	Empirical fit to CO_2 adsorption prefactor from Zent and Quinn (1995)	5.749×10^1	Unitless
ε	Obliquity	0–90	Degrees
ϵ_{CO_2}	Polar CO_2 ice emissivity	0.8	Unitless
ε_{reg}	Regolith emissivity	1.0	Unitless
F_{geo}	Geothermal energy flux	0.03	$W\,m^{-2}$
H	Atmospheric scale height	1,110	m
θ_S	Insolation incidence angle from nadir	Variable	Degrees
k_{reg}	**Regolith thermal conductivity**	**0.0837–2.0**	**$W\,m^{-1}\,K^{-1}$**
m_{atm}	Atmospheric CO_2 mass	presently 2.75×10^{16}; variable	kg
m_{cap}	Polar CO_2 ice cap mass	presently 2.68×10^{16}; variable	kg
$m_{n,obs}$	Observed mass of MCID layer number n	From observation	kg
$m_{n,syn}$	Model-predicted mass of MCID layer number n	Variable	kg
m_{reg}	Mass of CO_2 adsorbed in regolith	Variable	kg
m_{tot}	Total mass of Mars' exchangeable CO_2 on obliquity timescales	Variable	kg
$P_{eq,0}$	Pressure at the zero-elevation datum	Variable	Pa
$P_{eq,cap}$	Equilibrium pressure at the elevation of the upper surface of the polar CO_2 ice cap	Variable	Pa
ρ	Regolith density	837	$kg\,m^{-3}$
ρ_{CO_2}	Density of CO_2 ice	1,600	$kg\,m^{-3}$
S_{θ_S}	Incident surface insolation onto the regolith	Variable	$W\,m^{-2}$
$S_{\theta_S,\tau}$	Incident surface insolation onto the polar CO_2 ice	Variable	$W\,m^{-2}$
σ_B	Stefan-Boltzmann constant	5.67×10^{-8}	$W\,m^{-2}\,K^{-4}$
σ_{obs}	Observational uncertainty for each MCID layer mass	4.36×10^{15}	kg
T	Subsurface temperature T	Variable	K
T	Time	Variable	s
τ	Opacity over the polar cap	Variable	Unitless
$T_{eq,cap}$	Equilibrium temperature of the surface of the polar CO_2 ice cap	Variable	K
χ^2	MCMC stepwise chi-squared value	Variable	Unitless
Z	Subsurface depth	Variable	m
z_{base}	Elevation of the basal interface of the MCID with the underlying South Polar Layered Deposit	4,000	m
z_{reg}	**Active regolith thickness on obliquity timescales**	**1–1,000**	**m**

[1]The rows in bold are variable model inputs. MCMC, Markov Chain Monte Carlo; MCID, massive CO_2 ice deposit.

Data Availability Statement

Data tables containing the information in Figures 3–7 and the numerical modeling routine can be accessed in Buhler and Piqueux (2021).

References

Alwarda, R., & Smith, I. B. (2019). Mapping and characterization of the bounding layers of the CO_2 deposit in Planum Australe, Mars. *50th lunar planetary science conference, 2132*. USRA.

Athy, L. F. (1930). Density, porosity, and compaction of sedimentary rocks. *Bulletin of the American Association of Petroleum Geologists*, *14*, 1–24.

Ballou, E. V., Wood, P. C., Wydeven, T., Lehwalt, M. E., & Mack, R. E. (1978). Chemical interpretation of Viking Lander 1 life detection experiment. *Nature*, *271*, 644–645. https://doi.org/10.1038/271644a0

Bandfield, J. L., Edwards, C. S., Montgomery, D. R., & Brand, B. D. (2013). The dual nature of the martian crust: Young lavas and old clastic materials. *Icarus*, *222*, 188–199. https://doi.org/10.1016/j.icarus.2012.10.023

Bierson, C. J., Phillips, R. J., Smith, I. B., Wood, S. E., Putzig, N. E., Nunes, D., & Byrne, S. (2016). Stratigraphy and evolution of the buried CO2 deposit in the Martian south polar cap. *Geophysical Research Letters*, *43*, 4172–4179. https://doi.org/10.1002/2016gl068457

Binder, A. B., & Lange, M. A. (1980). On the thermal history, thermal state, and related tectonism of a moon of fission origin. *Journal of Geophysical Research*, *85*, 3194–3208. https://doi.org/10.1029/jb085ib06p03194

Buhler, P. B., Ingersoll, A. P., Ehlmann, B. L., Fassett, C. I., & Head, J. W. (2017). How the martian residual south polar cap develops quasi-circular and heart-shaped pits, troughs, and moats. *Icarus*, *286*, 69–93. https://doi.org/10.1016/j.icarus.2017.01.012

Buhler, P. B., Ingersoll, A. P., Piqueux, S., Ehlmann, B. L., & Hayne, P. O. (2020). The origin of Mars' south polar massive CO_2 ice deposit from co-evolution with Mars' atmosphere. *Nature Astronomy*, 1–8.

Buhler, P. B., & Piqueux, S. (2021). *Data Tables Buhler Piqueux JGR 2021*. figshare. Dataset. https://doi.org/10.5194/tc-2021-34-rc2

Clauser, C., & Huenges, E. (1995). Thermal conductivity of rocks and minerals. In T. J. Ahrens (Ed.), *Rock physics and phase relations: A handbook of physical constants* (pp. 105–126). Washington, DC: American Geophysical Union.

Clifford, S. M. (1991). The role of thermal vapor diffusion in the subsurface hydrologic evolution of Mars. *Geophysical Research Letters*, *18*, 2055–2058. https://doi.org/10.1029/91gl02469

Clifford, S. M. (1993). A model for the hydrologic and climatic behavior of water on Mars. *Journal of Geophysical Research*, *98*, 10–973. https://doi.org/10.1029/93je00225

Colaprete, A., Barnes, J. R., Haberle, R. M., Hollingsworth, J. L., Kieffer, H. H., & Titus, T. N. (2005). Albedo of the south pole on Mars determined by topographic forcing of atmosphere dynamics. *Nature*, *435*, 184–188. https://doi.org/10.1038/nature03561

Dehant, V., Banerdt, B., Lognonné, P., Grott, M., Asmar, S., Biele, J., et al. (2012). Future Mars geophysical observatories for understanding its internal structure, rotation, and evolution. *Planetary and Space Science*, *68*, 123–145. https://doi.org/10.1016/j.pss.2011.10.016

Edwards, C. S., Bandfield, J. L., Christensen, P. R., & Fergason, R. L. (2009). Global distribution of bedrock exposures on Mars using THEMIS high-resolution thermal inertia. *Journal of Geophysical Research*, *114*. E11001. https://doi.org/10.1029/2009je003363

Edwards, C. S., Bandfield, J. L., Christensen, P. R., & Rogers, A. D. (2014). The formation of infilled craters on Mars: Evidence for widespread impact induced decompression of the early martian mantle? *Icarus*, *228*, 149–166. https://doi.org/10.1016/j.icarus.2013.10.005

Edwards, C. S., Christensen, P. R., & Hamilton, V. E. (2008). Evidence for extensive olivine-rich basalt bedrock outcrops in Ganges and Eos chasmas, Mars. *Journal of Geophysical Research*, *113*, E11003. https://doi.org/10.1029/2008je003091

Fanale, F. P., & Cannon, W. A. (1971). Adsorption on the Martian regolith. *Nature*, *230*, 502–504. https://doi.org/10.1038/230502a0

Fanale, F. P., Salvail, J. R., Bruce Banerdt, W., & Steven Saunders, R. (1982). Mars: The regolith-atmosphere-cap system and climate change. *Icarus*, *50*, 381–407. https://doi.org/10.1016/0019-1035(82)90131-2

Golombek, M., Grott, M., Kargl, G., Andrade, J., Marshall, J., Warner, N., et al. (2018). Geology and physical properties investigations by the insight lander. *Space Science Reviews*, *214*, 84. https://doi.org/10.1007/s11214-018-0512-7

Golombek, M., Kass, D., Williams, N., Warner, N., Daubar, I., Piqueux, S., et al. (2020). Assessment of insight landing site predictions. *Journal of Geophysical Research: Planets*, *125*, e2020JE006502. https://doi.org/10.1029/2020JE006502

Golombek, M., Kipp, D., Warner, N., Daubar, I., Fergason, R., Kirk, R. L., et al. (2017). Selection of the insight landing site. *Space Science Reviews*, *211*, 5–95. https://doi.org/10.1007/s11214-016-0321-9

Guo, X., Richardson, M. I., Soto, A., & Toigo, A. (2010). On the mystery of the perennial carbon dioxide cap at the south pole of Mars. *Journal of Geophysical Research*, *115*, 1–13. https://doi.org/10.1029/2009je003382

Gyalay, S., Nimmo, F., Plesa, A. C., & Wieczorek, M. (2020). Constraints on thermal history of Mars from depth of pore closure below insight. *Geophysical Research Letters*, *47*, e2020GL088653. https://doi.org/10.1029/2020gl088653

Haberle, R. M., Forget, F., Colaprete, A., Schaeffer, J., Boynton, W. V., Kelly, N. J., & Chamberlain, M. A. (2008). The effect of ground ice on the Martian seasonal CO_2 cycle. *Planetary and Space Science*, *56*, 251–255. https://doi.org/10.1016/j.pss.2007.08.006

Haberle, R. M., Murphy, J. R., & Schaeffer, J. (2003). Orbital change experiments with a Mars general circulation model. *Icarus*, *161*, 66–89. https://doi.org/10.1016/s0019-1035(02)00017-9

Hayne, P. O., Paige, D. A., Schofield, J. T., Kass, D. M., Kleinbohl, A., Heavens, N. G., & McCleese, D. J. (2011). Carbon dioxide snow clouds on Mars: South polar winter observations by the Mars climate sounder. *Journal of Geophysical Research*, *117*, E08014. https://doi.org/10.1029/2011JE004040

Head, J. W., Mustard, J. F., Kreslavsky, M. A., Milliken, R. E., & Marchant, D. R. (2003). Recent ice ages on Mars. *Nature*, *426*, 797–802. https://doi.org/10.1038/nature02114

Head, J. W., Neukum, G., Neukum, G., Jaumann, R., Hiesinger, H., Hauber, E., et al. (2005). Tropical to mid-latitude snow and ice accumulation, flow and glaciation on Mars. *Nature*, *434*, 346–351. https://doi.org/10.1038/nature03359

Hess, S. L., Ryan, J. A., Tillman, J. E., Henry, R. M., & Leovy, C. B. (1980). The annual cycle of pressure on mars measured by Viking landers 1 and 2. *Geophysical Research Letters*, *7*, 197–200. https://doi.org/10.1029/gl007i003p00197

Holt, J. W., Safaeinili, A., Plaut, J. J., Head, J. W., Phillips, R. J., Seu, R., et al. (2008). Radar sounding evidence for buried glaciers in the southern mid-latitudes of Mars. *Science*, *322*, 1235–1238. https://doi.org/10.1126/science.1164246

Hourdin, F., Le Van, P., Forget, F., & Talagrand, O. (1993). Meteorological variability and the annual surface pressure cycle on Mars. *Journal of the Atmospheric Sciences*, *50*, 3625–3640. https://doi.org/10.1175/1520-0469(1993)050<3625:mvatas>2.0.co;2

Ingersoll, A. P. (1970). Mars: Occurrence of liquid water. *Science*, *168*, 972–973. https://doi.org/10.1126/science.168.3934.972

Jakosky, B. M., Brain, D., Chaffin, M., Curry, S., Deighan, J., Grebowsky, J., et al. (2018). Loss of the Martian atmosphere to space: Present-day loss rates determined from MAVEN observations and integrated loss through time. *Icarus*, *315*, 146–157

Kieffer, H. H. (2013). Thermal model for analysis of Mars infrared mapping. *Journal of Geophysical Research*, *118*, 451–470. https://doi.org/10.1029/2012je004164

Kieffer, H. H., Martin, T. Z., Peterfreund, A. R., Jakosky, B. M., Miner, E. D., & Palluconi, F. D. (1977). Thermal and albedo mapping of Mars during the Viking primary mission. *Journal of Geophysical Research*, *82*(, 4249–4291. https://doi.org/10.1029/js082i028p04249

Kreslavsky, M. A., & Head, J. W. (2011). Carbon dioxide glaciers on Mars: Products of recent low obliquity epochs (?). *Icarus*, *216*, 111–115. https://doi.org/10.1016/j.icarus.2011.08.020

Laskar, J, Correia, A. C. M., Gastineau, M., Joutel, F., Levrard, B., & Robutel, P. (2004). Long term evolution and chaotic diffusion of the insolation quantities of Mars. *Icarus*, *170*, 343–364. https://doi.org/10.1016/j.icarus.2004.04.005

Lognonné, P., Banerdt, W. B., Pike, W. T., Giardini, D., Christensen, U., Garcia, R. F., et al. (2020). Constraints on the shallow elastic and anelastic structure of Mars from insight seismic data. *Nature Geoscience*, *13*, 213–220

Madeleine, J.-B., Forget, F., Head, J. W., Levrard, B., Montmessin, F., & Millour, E. (2009). Amazonian northern mid-latitude glaciation on Mars: A proposed climate scenario. *Icarus*, *203*, 390–405. https://doi.org/10.1016/j.icarus.2009.04.037

Manning, C. V., Bierson, C., Putzig, N. E., & McKay, C. P. (2019). The formation and stability of buried polar $CO2$ deposits on Mars. *Icarus*, *317*, 509–517. https://doi.org/10.1016/j.icarus.2018.07.021

Mellon, M., Jakosky, B. M., Kieffer, H. H., & Christensen, P. R. (2000). High-resolution thermal inertia mapping from the Mars global surveyor thermal emission spectrometer. *Icarus*, *148*, 437–455. https://doi.org/10.1006/icar.2000.6503

Montabone, L., Forget, F., Millour, E., Wilson, R. J., Lewis, S. R., Cantor, B., et al. (2015). Eight-year climatology of dust optical depth on Mars. *Icarus*, *251*, 65–95. https://doi.org/10.1016/j.icarus.2014.12.034

Morgan, P., Grott, M., Knapmeyer-Endrun, B., Golombek, M., Delage, P., Lognonné, P., et al. (2018). A pre-landing assessment of regolith properties at the insight landing site. *Space Science Reviews*, *214*, 1–47. https://doi.org/10.1007/s11214-018-0537-y

Neugebauer, G., Miinch, G., Kieffer, H., Chase, S. C. J., Jr, & Miner, E. (1971). Mariner 1969 infrared radiometer results: Temperatures and thermal properties of the Martian surface. *Astronomical Journal*, *76*, 719–749. https://doi.org/10.1086/111189

Nielsen, M. E., & Fisk, M. R. (2010). Surface area measurements of marine basalts: Implications for the subseafloor microbial biomass. *Geophysical Research Letters*, *37*. https://doi.org/10.1029/2010gl044074

Owen, T., Biemann, K., Rushneck, D. R., Biller, J. E., Howarth, D. W., & Lafleur, A. L. (1977). The composition of the atmosphere at the surface of Mars. *Journal of Geophysical Research*, *82*, 4635–4639. https://doi.org/10.1029/js082i028p04635

Oyama, V. I., & Berdahl, B. J. (1977). The Viking gas exchange experiment results from Chryse and Utopia surface samples. *Journal of Geophysical Research*, *82*, 4669–4676. https://doi.org/10.1029/js082i028p04669

Paige, D. A., & Ingersoll, A. P. (1985). Annual heat balance of martian polar caps: Viking observations. *Science*, *228*, 1160–1168. https://doi.org/10.1126/science.228.4704.1160

Palluconi, F., & Kieffer, H. H. (1981). Thermal inertia mapping of Mars from 60°S to 60°N. *Icarus*, *45*, 415–426. https://doi.org/10.1016/0019-1035(81)90044-0

Phillips, R. J., Davis, B. J., Tanaka, K. L., Byrne, S., Mellon, M. T., Putzig, N. E., et al. (2011). Massive CO_2 ice deposits sequestered in the south polar layered deposits of Mars. *Science*, *332*, 838–841. https://doi.org/10.1126/science.1203091

Plaut, J. J., Picardi, G., Safaeinili, A., Ivanov, A. B., Milkovich, S. M., Cicchetti, A., et al. (2007). Subsurface radar sounding of the south polar layered deposits of Mars. *Science*, *316*, 92–95. https://doi.org/10.1126/science.1139672

Putzig, N. E., Smith, I. B., Perry, M. R., Foss, F. J., II, Campbell, B. A., Phillips, R. J., & Seu, R. (2018). Three-dimensional radar imaging of structures and craters in the Martian polar caps. *Icarus*, *308*, 138–147. https://doi.org/10.1016/j.icarus.2017.09.023

Richardson, M. I., & Mischna, M. A. (2005). Long-term evolution of transient liquid water on Mars. *Journal of Geophysical Research: Planets*, *110*. https://doi.org/10.1029/2004je002367

Robertson, E. C. (1988). *Thermal properties of rocks. USGS geological survey open-file report* (pp. 88–441). USGS.

Rogers, A. D., Warner, N. H., Golombek, M. P., Head, J. W., & Cowart, J. C. (2018). Areally extensive surface bedrock exposures on Mars: Many are clastic rocks, not lavas. *Geophysical Research Letters*, *45*(4), 1767–1777. https://doi.org/10.1002/2018gl077030

Schmoker, J. W., & Gautier, D. L. (1988). Sandstone porosity as a function of thermal maturity. *Geology*, *16*, 1007–1010. https://doi.org/10.1130/0091-7613(1988)016<1007:spaafo>2.3.co;2

Schubert, G., Solomon, S. C., Turcotte, D. L., Drake, M. J., & Sleep, N. H. (1992). Origin and thermal evolution of Mars. In H. H. Kieffer, B. M. Jakosky, C. W. Snyder, & M. S. Matthews (Eds.), *Mars* (pp. 147–183). University of Arizona Press.

Smith, I. B., Schlegel, N., Larour, E., Isola, I., Buhler, P., Putzig, N. E., & Greve, R. (2021). CO_2 glaciers on the south polar layered deposits of Mars. *Lunar and planetary science conference abstract #2573*. USRA. https://doi.org/10.1201/9780429332432

Thomas, P. C., Calvin, W., Cantor, B., Haberle, R., James, P. B., & Lee, S. W. (2016). Mass balance of Mars' residual south polar cap from CTX images and other data. *Icarus*, *268*, 118–130. https://doi.org/10.1016/j.icarus.2015.12.038

Toon, O. B., Pollack, J. B., Ward, W., Burns, J. A., & Bilski, K. (1980). The astronomical theory of climatic change on Mars. *Icarus*, *44*, 552–607. https://doi.org/10.1016/0019-1035(80)90130-x

Warner, N. H., Golombek, M. P., Sweeney, J., Fergason, R., Kirk, R., & Schwartz, C. (2017). Near surface stratigraphy and regolith production in southwestern Elysium Planitia, Mars: Implications for Hesperian-Amazonian terrains and the insight lander mission. *Space Science Reviews*, *211*, 147–190. https://doi.org/10.1007/s11214-017-0352-x

Zent, A. P., & Quinn, R. C. (1995). Simultaneous adsorption of $CO2$ and $H2O$ under Mars-like conditions and application to the evolution of the Martian climate. *Journal of Geophysical Research*, *100*, 5341–5349. https://doi.org/10.1029/94je01899

Zuber, M. T., Solomon, S. C., Phillips, R. J., Smith, D. E., Tyler, G. L., Aharonson, O., et al. (2000). Internal structure and early thermal evolution of Mars from Mars global surveyor topography and gravity. *Science*, *287*, 1788–1793. https://doi.org/10.1126/science.287.5459.1788